NANO · MICRO small
www.small-journal.com

Coffee Ring–Inspired Approach toward Oriented Self-Assembly of Biomimetic Murray MOFs as Sweat Biosensor

*Zhengyun Wang, Ting Liu, Yang Yu, Muhammad Asif, Ning Xu, Fei Xiao, and Hongfang Liu**

The emergence of metal–organic frameworks (MOFs) has sparked intensive attention and opened up the possibility of "crystal engineering." However, low conductivity, slow diffusion of guest molecules, as well as powder forms always hinder the development of MOF application, especially for biosensors and bioelectronics. Herein, a coffee ring–inspired strategy toward oriented self-assembly of a biomimetic MOF film following Murray's law is proposed, which can effectively reduce the transfer resistance. The approach includes two types of self-assembly, evaporation-driven and heteroepitaxy self-assembly, and endows the centimeter-expanded MOF film with oriented macropores, mesopores, and micropores. The Murray MOF network enables greatly enhanced electrons and mass transfer efficiency for electrochemical sensing. Also, the newly discovered lactate and glucose sensing abilities in a wide pH hold striking potential in new generation of wearable sweat biosensors, miniature bioelectronics, and lab-on-a-chip devices.

1. Introduction

Recent years have witnessed a spurt progress in metal–organic frameworks (MOFs) that opens up the possibility of "crystal engineering" driven by their unprecedented structures and remarkable performances.[1–5] MOFs defined as a class of nanoporous materials are composed of periodical inorganic metal ions/clusters and bridged organic linkers. Modular architecture of MOFs allows for regulation of network topology, structure metrics, along with coordination chemistry, which holds striking promise in extensive applications such as sensing, catalysis, gas storage, energy, and molecular separations.[6,7] Nevertheless, given the relevance between reaction parameters and synthetic outcome, it can always be hard to predict the size, morphology, distribution, and orientation of targeted MOFs.[8,9] More importantly, progress in these applications especially for electrochemical devices and biosensing system has been restricted by poor conductivity, slow diffusion and transfer of guest molecules, and powdered form.[10,11] In addition, it has been acknowledged as an indispensable measure to process MOF nanocrystals into centimeter-level film for their integrated functional electronics.[12] Based on these, a significant step to achieve the MOFs' potentiality in electronics is exploration of continuous, oriented films with centimeter dimensions which allows for structural superiority and performance enhancement, facilitating fast molecules and electron transfer. At this time, a thought-provoking question arises: how to endow large-area MOF film with high mass, electron transfer, and activity? The factor at play in tough to overcome this elegant challenge is that the abovementioned deficiencies of MOFs are not able to be easily solved through rational structure design. Nonetheless, we still profoundly believe that we can seek inspiration in natural system for preparing MOF film with mass, electron high transfer efficiency.

Numerous living organisms such as vascular, respiratory systems, and leaf veins have been endowed with hierarchically porous networks by natural evolution.[13–16] These networks initiate with macropores and their subpore sizes decrease in a regular manner along multiscales and terminate in constant sizes.[17] This type of natural porous network that follows Murray's law can minimize transport resistance of the whole pores, further enhancing the mass transfer, described as Murray network.[18] For instance, in the leaf veins, the pore volume remains constant across every pathway to maximize the flow conductance due to the constant of sum of the radii cubed, proportional to the photosynthesis.[17] For breathing of insects, the surface area of tracheal pores remains constant across diffusion branch because of the constant of sum of the radii squared, facilitating the gas diffusion.[14] On account of the abovementioned advantages, a fascinating biomimetic strategy to overcome the defects of MOFs is mimicking the natural Murray network and designing hierarchical MOFs with maximized transfer properties. To mimic the MOF morphology into the Murray network, in view of different dimensional-connected channels of natural Murray structure, the micropores of MOF unit could be as the minimum subchannels and the space between adjacent MOFs could be connected secondary

Dr. Z. Wang, T. Liu, Dr. Y. Yu, Dr. M. Asif, Dr. N. Xu, Prof. F. Xiao, Prof. H. Liu
Key Laboratory of Material Chemistry for Energy Conversion and Storage Ministry of Education
Hubei Key Laboratory of Material Chemistry and Service Failure
School of Chemistry and Chemical Engineering
Huazhong University of Science and Technology
Wuhan 430074, P. R. China
E-mail: liuhf@hust.edu.cn

The ORCID identification number(s) for the author(s) of this article can be found under https://doi.org/10.1002/smll.201802670.

DOI: 10.1002/smll.201802670

and first channels, confirming that the proposed Murray MOF network concept is highly reasonable. But another question arises: which approach will bestow on MOF film hierarchical porous networks? Current great construction methods of MOFs including hydrothermal synthesis,[19] microwave fabrication,[20] monolayer self-assembly,[21] electrochemical techniques,[22] gel-layer preparation,[23] and layer-by-layer methodology[24] are very useful when combined with crystal engineering techniques. But, they cannot allow for precisely manipulation of oriented hierarchical porous MOF film,[11,18] we still need to seek inspiration from new perspectives. Imagine this scene, when a drop of coffee dries on a paper, it leaves a ring-like deposit along the circle perimeter, forming "coffee ring" on the paper surface after complete evaporation.[25,26] It is highly desirable to achieve large-area macropores and mesopores with oriented spatial arrangements in MOF film through this evaporation-driven process. Furthermore, we might as well further create micropores on these "coffee rings" through lattice match design to realize orientation self-assembly to connect with mesopores and obtain the final MOF film with Murray network. Herein, our work proposes a coffee ring–inspired approach to shed light on this issue, toward oriented self-assembly of biomimetic MOF film, as shown in **Scheme 1**. In order to mimic the Murray network, well-defined $Cu(OH)_2$ nanowires as the primary building blocks are used as precursor for generating oriented $Cu_2(NDC)_2$ film on a pencil drawing hydrophobic paper (PDHP). A fascinating discovery in our work is that centimeter-sized extended hierarchical pores of $Cu_2(NDC)_2$ film occur via evaporation-driven self-assembly and heteroepitaxial growth process.

We envision that the biomimetic Murray MOFs film would possess fast transfer ability of mass and electrons, which is appropriate to applications in sweat biosensors and bioelectronics. Wearable sweat sensing is a burgeoning field which guides a promising future for personalized health, fitness, and diagnostic assessment.[27–32] Sweat lactate ($\approx 10 \times 10^{-3}$ M) is capable to serve as the pressure ischemia biomarkers, reflecting compromise of tissue viability and insufficient oxidative metabolism.[33,34] Sweat glucose (0.28×10^{-3}–1.11×10^{-3} M) has been discovered in good relationship with blood glucose (4×10^{-3}–8×10^{-3} M), thus can be utilized for treatment of glycometabolism related disease.[35,36] Current sweat sensors based on enzyme system always suffer from long-time stability and high cost of lactate and glucose oxidase. Consequently, the increasing demand for new generation of sweat sensors calls for the exploration of nonenzymatic nanomaterials with excellent sensing performances as well as and long-time stability and low cost. The proposed porous Murray $Cu_2(NDC)_2$/PDHP film composed of coadjacent passways spans the macroporous, mesoporous, and microporous dimensions and exhibits remarkable electrochemical sensing performances toward lactate and glucose. The newly found sensing function of $Cu_2(NDC)_2$/PDHP is of great positive significance for nonenzymatic electrochemical lactate detection. More interestingly, the $Cu_2(NDC)_2$/PDHP film still manifests admirable sensing ability in the acid media, whereas it is often hard to play a role in glucose sensing for Cu-based materials in acid media because of its oxidation mechanism. In virtue of improved mass exchange and electron transfer with high efficiency, $Cu_2(NDC)_2$/PDHP has been applied to human perspiration sensing platform

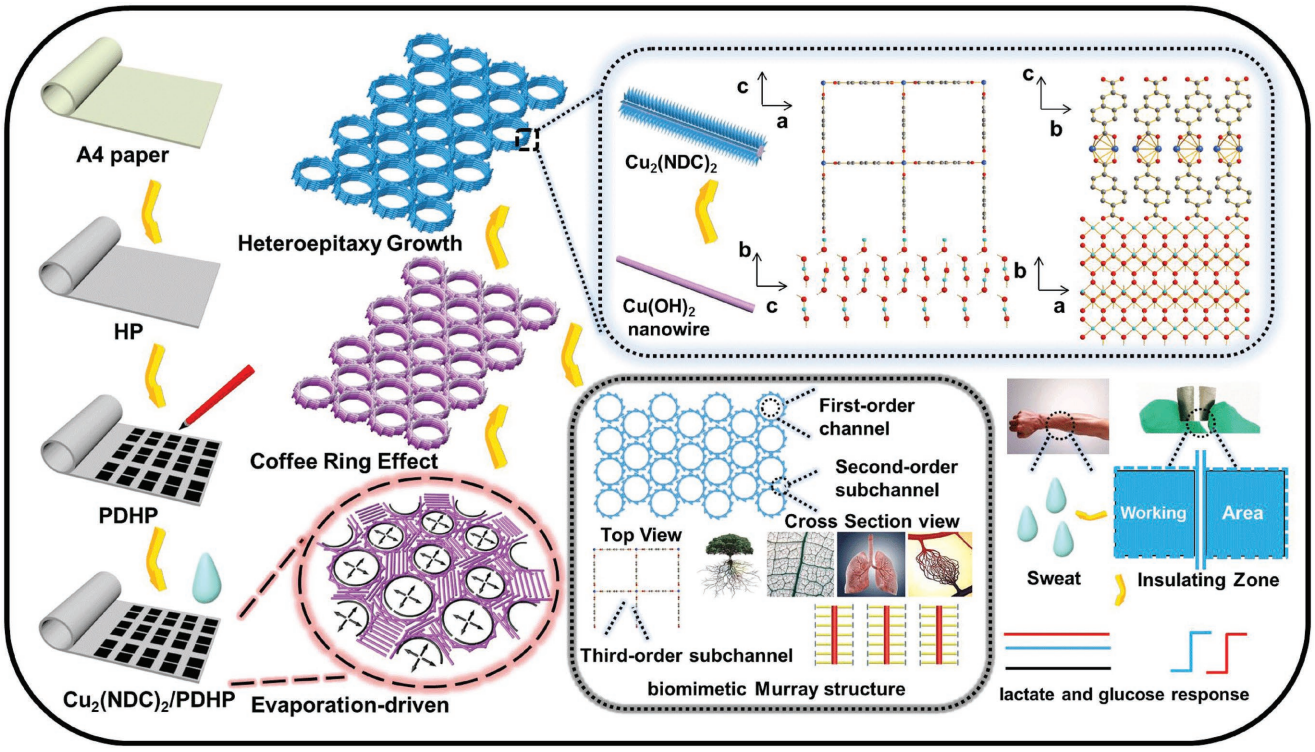

Scheme 1. The fabrication process of biomimetic Murray $Cu_2(NDC)_2$/PDHP.

for the first time. We believe our work would pave the way for pursuing biomimetic, oriented, and hierarchical porous MOF film with optimized performances for more MOF-based applications.

2. Results and Discussion

2.1. Morphological and Structural Characterization

The $Cu_2(NDC)_2$/PDHP fabrication process can be divided into two dependent parts, preparation of substrate and construction of MOF film, as depicted in Scheme 1. **Figure 1**A displays that common A4 printing paper is composed of cellulose fibers (5 μm diameters). It can be clearly observed that the cellulose fibers via hydrophobic treatment are entirely covered by uniform and contact hinge-like polypropylene (PP) (Figure 1B), which makes A4 paper become hydrophobic. After pencil drawing, the surface of PDHP becomes relatively smooth due to ordered and compact graphite framework derived from 9B pencil, as shown in Figure 1C. The insets from Figure 1A–C compare the contact angle variations of A4 paper, HP, and PDHP, demonstrating successful surface property transformation of the substrate from hydrophilicity to hydrophobicity. Figure 1D exhibits the precursor network realized via coffee ring effect, that is, evaporation-driven self-assembly of $Cu(OH)_2$ nanowires. During this process, extensive areas with open, uniform, and well-defined holes with diameter of 1 μm are distinctly observed on the surface of PDHP, spaced with thin net-like walls across the rims of circle. Under the higher magnification, these rings and thin walls are found to be constructed from $Cu(OH)_2$ nanowires (Figure 1E,F). After immersing in 2,6-naphthalenedicarboxylic acid (H_2(NDC)) solution for 30 min, external-ring macroporous space still maintains after heteroepitaxy growth (Figure 1G). Figure 1H,I exhibits that $Cu_2(NDC)_2$ composed of crystals are orthogonal to the $Cu(OH)_2$ nanowires. The morphology change fully indicates the successful conversion of MOFs. After oriented heteroepitaxy growth along the axis of $Cu(OH)_2$, the mesopores are inter-nanowire spaces created by adjacently arranged $Cu_2(NDC)_2$, thus the interwire mesoporous channels still retain. The whole formation process of this kind of unique, biomimetic Murray MOF network can be summarized: for precursor, a square planar complex $[Cu(NH_3)_4]^{2+}$ will form in $CuSO_4$ solution upon addition of NH_3OH for obtaining $Cu(OH)_2$ nanowires. The fact that the growth of the layer-structured orthorhombic $Cu(OH)_2$ is much quicker than that of any other direction causes forming 1D morphology as NaOH solution is added. This step is essential to the construction of our oriented self-assembly of biomimetic Murray MOFs. When the dichloromethane drop containing high content of $Cu(OH)_2$ nanowires dries on PDHP surface, the contact line of the droplet is pined in virtue of the reduced static frictional force originating from modified hydrophobic interface. In addition, dichloromethane with lower boiling point will easily evaporate in the air at room temperature. Evaporation drives dichloromethane to lose at the droplet's edge and would also draw new dichloromethane molecules from the center of the droplet to replace previous vacancy. It is noteworthy that the flow carries not only fluid but also $Cu(OH)_2$ from the center to the edge of the droplet, leading to $Cu(OH)_2$ nanowires formed rings at the edge after complete evaporation. Hence, spontaneous evaporation of dichloromethane in plenty of these small region induces many macropores to form and $Cu(OH)_2$ nanowires are pushed to aggregate the edges of these macropores, resulting in forming thin walls composed of numerous mesopores between nanowires. For the next self-assembly step, since $Cu(OH)_2$ is crystallized with 2.95, 10.59, 5.26 Å for *a*, *b*, *c* and the organic linker H_2(NDC) possesses closed lattice with $Cu(OH)_2$, oriented heteroepitaxy growth occurs, resulting in copper paddle-wheel units in alignment with *a* and *c* crystallographic axes of substrate. Finally, $Cu_2(NDC)_2$ film finishes orienting along the *a*, *b*, and *c* axes through $Cu(OH)_2$ conversion. Heteroepitaxial growth between the metal hydroxide lattice and organic linker structure ensures the final oriented and precise matching. Oriented self-assembly ensures perfect reservation of mesopores, as well as macropores. Moreover, heteroepitaxy growth creates microporous channels because $Cu_2(NDC)_2$ itself is a kind of microporous MOFs. The mesopores are connected with micropores and macropores, which can be regarded as biomimetic Murray network. The scanning electron microscope (SEM) elementary mapping images of C, O, Cu from Figure 1J–M also demonstrate that the hierarchical porous $Cu_2(NDC)_2$ films are uniformly and well-orderly distributed on the PDHP. Especially, the C element distributed in coffee ring indicates the successful conversion of MOFs, whereas C element does not exist in $Cu(OH)_2$. These results also illustrate that oriented biomimetic Murray MOF film would be formed through two-step self-assembly, driven by coffee ring effect and heteroepitaxy growth, further confirming our structure prediction.

Fourier transform infrared spectrum (FTIR) is performed to probe the composition of substrate and the results are represented in **Figure 2**A. The weak peaks in A4 paper at 3380, 2950, 1425, and 1020 cm^{-1} are assigned to O—H and $-CH_2-$ stretching vibrations in $C_{10}H_{16}O$, C—O, and CO_3^{2-} bending vibrations in $CaCO_3$, respectively. These substances always exist in printing paper for insect prevention. New peaks at 2980, 1490, and 1380 cm^{-1} are clearly recognized in HP, corresponding to $-CH_3$ stretching, $-CH_2-$ bending, and $-CH_3$ deformable vibrations, respectively. Compared to HP, PDHP displays weaker transmittance owing to dense graphic drawn on the surface. These indicate the successful modification of the substrate for oriented self-assembly of MOFs.

X-ray diffraction (XRD) is performed to investigate the phase structure of the A4 paper, HP, PDHP, $Cu(OH)_2$/PDHP, and $Cu_2(NDC)_2$/PDHP (Figure 2B). The first broad peak in A4 paper at 15.6° is attributed to $C_{10}H_{16}O$, and this result is also consistent with FTIR. The diffraction peaks at 23.1°, 29.4°, 35.9°, 39.4°, 42.8°, 43.9°, 48.5° are attributed to crystalline $CaCO_3$ in A4 paper originating from raw materials for paper making. After hydrophobicity modification, the intensity of diffraction peaks in HP becomes weak due to dense coverage of PP. For PDHP, the peak at around 26.4° is assigned to carbon (002) facets, corresponding to the graphite from pencil. The XRD patterns of $Cu(OH)_2$/PDHP display that the peaks at 16.7°, 23.8°, and 34.1°[37] assign to the (020), (021), and (002) facets of $Cu(OH)_2$ nanowires. Through heteroepitaxy growth, the peaks at 7.0°, 13.5°, and 21.5° are corresponding to pure $Cu_2(NDC)_2$, which demonstrates oriented MOFs self-assembly.

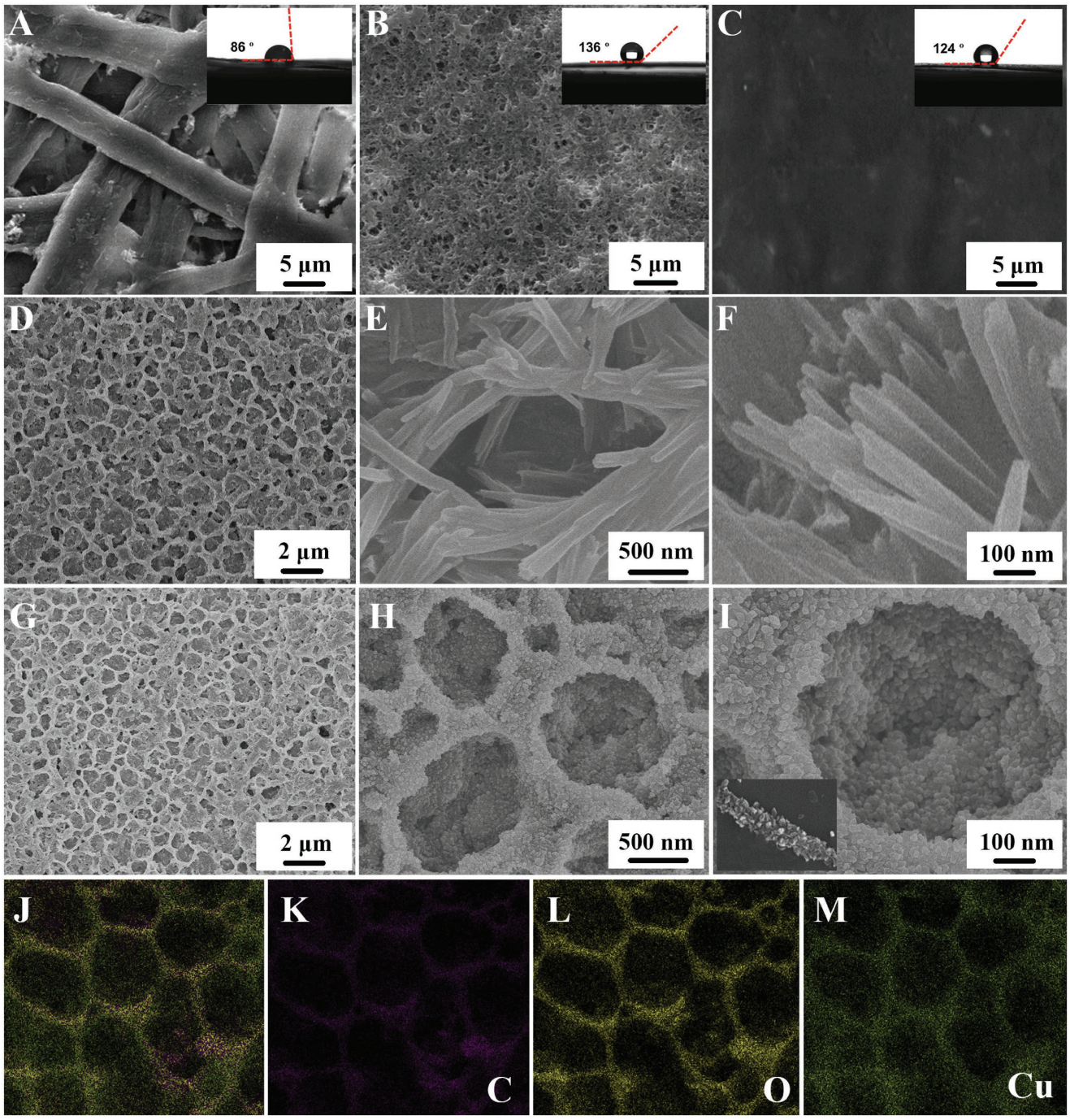

Figure 1. SEM of A) A4 paper, B) HP, and C) PDHP. The insets are the respective contact angles. SEM of D–F) coffee ring formed by $Cu(OH)_2$ nanowires on PDHP; G–I) coffee ring formed by oriented $Cu_2(NDC)_2$ on PDHP. The inset of (I) is single $Cu_2(NDC)_2$ after heteroepitaxy growth on $Cu(OH)_2$ nanowire. J–M) SEM mapping of C, O, Cu elements.

X-ray photoelectron spectroscopy (XPS) is further employed to analyze the elemental chemical states of $Cu_2(NDC)_2$/PDHP and C, O, Cu elements are determined (Figure 2C). The C 1s spectra can be deconvoluted into three peaks at 284.6, 286.5, and 288.2 eV, which are consistent with C—C/C=C, C—O, and C=O, respectively (Figure 2D), consistent with the previous reports.[38] The C—C/C=C, C—O, and C=O peaks originate from the linker of $Cu_2(NDC)_2$, corresponding to the carbon and oxygen in the benzene ring and the carboxyl group. The C 1s peak change from $Cu(OH)_2$/PDHP to $Cu_2(NDC)_2$/PDHP also demonstrates the presence of MOFs (see XPS of $Cu(OH)_2$/PDHP in the Supporting Information). Figure 2E represents Cu $2p_{3/2}$ and Cu $2p_{1/2}$ peaks of $Cu_2(NDC)_2$ at 933.5 and 954.9 eV. The high resolution Cu 2p spectrum exhibits two small satellite peaks at 943.5 and 938.9 eV,[39] originating from $Cu_2(NDC)_2$. The C, H, O, Cu, and Ca mass

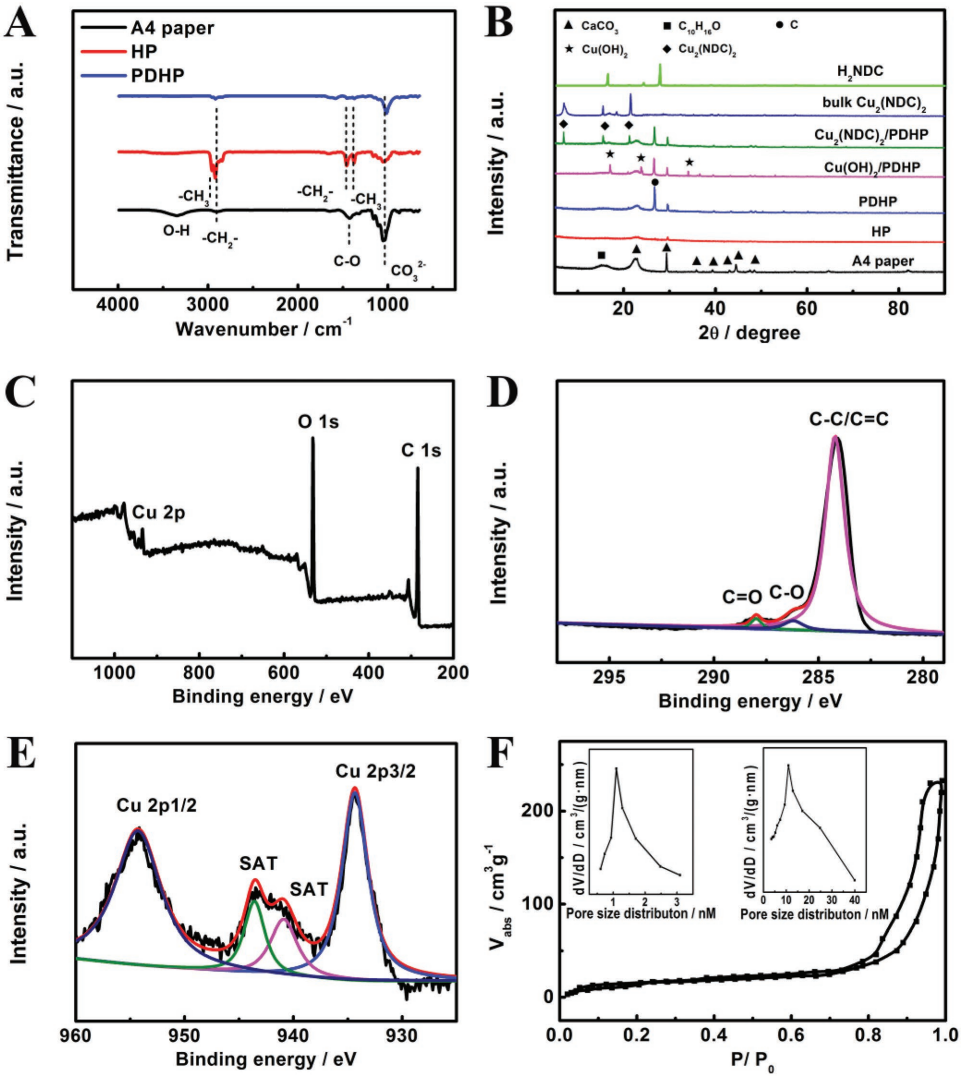

Figure 2. A) FTIR. B) XRD patters. C–E) XPS spectrums. F) N_2 adsorption–desorption isotherms and pore size distributions.

percentages in $Cu_2(NDC)_2$/PDHP analyzed by elemental analysis (EA) and inductively coupled plasma mass spectrometry (ICP-MS) characterization are 51.48%, 2.01%, 23.29%, 21.02%, and 2.20%, respectively. The C, H, O, Cu, and Ca mass percentages in $Cu(OH)_2$/PDHP are 51.12%, 1.85%, 23.08%, 21.93%, and 2.02%. Due to existence of C and O elements in PDHP substrate, there is no significant change in the elemental composition from $Cu(OH)_2$/PDHP to $Cu_2(NDC)_2$/PDHP (see Table S3 in the Supporting Information).

The Murray regularity of the synthesized $Cu_2(NDC)_2$/PDHP structure is further analyzed by nitrogen adsorption. N_2 isothermal adsorption–desorption curve using the Barrett–Joyner–Halenda model analysis proves mesopore with a 10 nm mean size, assigning to inter-nanowires space created by adjacently arranged $Cu_2(NDC)_2$ (Figure 2F). On the other hand, micropores with 1.1 nm size within $Cu_2(NDC)_2$ are observed, attributed to natural micropores in $Cu_2(NDC)_2$. For Murray regularity, the size of first channel should be larger than that of second channel and the size of second channel should be larger than that of third channel. For our materials, we can obtain: the macropore size > mesopore size > micropore size. The results further confirm that $Cu_2(NDC)_2$/PDHP possesses high specific surface area (396.6 $m^2\ g^{-1}$) and the pore distribution is very close to Murray's regularity[18] (see details in the Supporting Information).

2.2. Electrochemical Behavior of $Cu_2(NDC)_2$/PDHP

$[Fe(CN)_6]^{3-/4-}$ is first adopted to explore the electrochemical performances of $Cu_2(NDC)_2$/PDHP as well as control samples including A4 paper, HP, PDHP, and bulk $Cu_2(NDC)_2$ powders. **Figure 3**A summarizes electrochemical impedance spectroscopy (EIS) results of the corresponding materials. Insulating A4 paper shows a huge Faradaic charge transfer resistance (R_{ct}), which retains approximately constant in HP because of no conjugated structure in PP. The R_{ct} of HP reduces to 200 Ω in PDHP owing to graphitic sheets of sp^2 bonds.

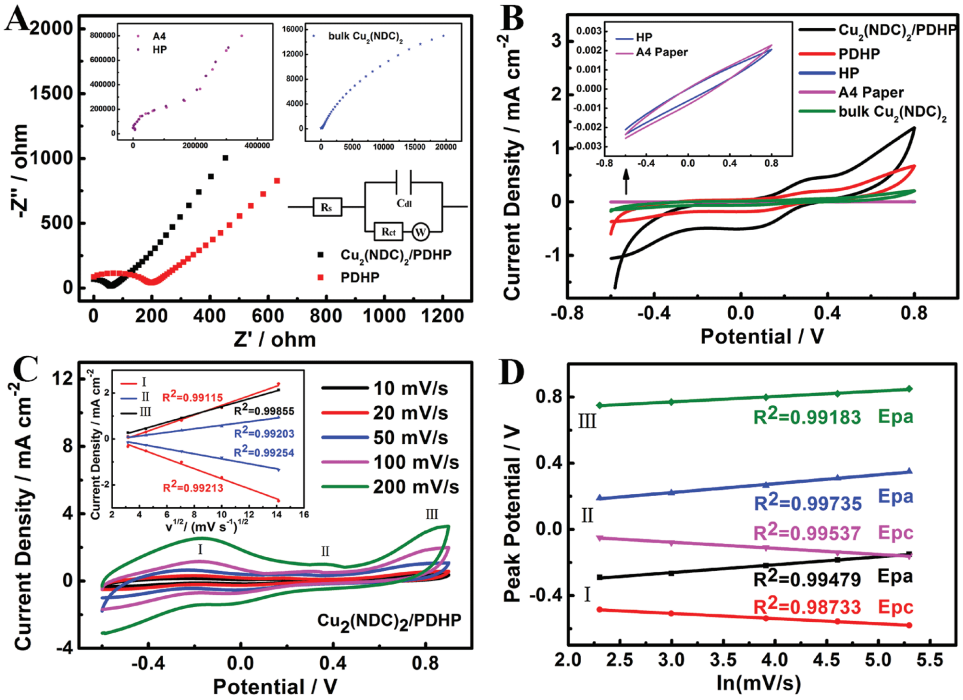

Figure 3. A) Nyquist plots (0.1–10^5 Hz) and B) CV curves (50 mV s^{-1}) of different samples with 1.0×10^{-3} M $K_3Fe(CN)_6$ and 1.0×10^{-3} M $K_4Fe(CN)_6$. C) CV of $Cu_2(NDC)_2$/PDHP in simulated sweat (pH = 8.0) from 10 to 200 mV s^{-1}. Inset: plot of peak current versus square root of the scan rate. D) Linear fitting of the peak potential versus lnν.

Bulk $Cu_2(NDC)_2$ possesses a large R_{ct} of 1800 Ω in virtue of its limited conductivity. But interestingly, the R_{ct} of $Cu_2(NDC)_2$/PDHP reduces to 90 Ω, further indicating boosted electron transfer in hierarchical Murray network. As cyclic voltammetry (CV) shown in Figure 3B, fusiform shapes with no redox peaks are observed on the A4 paper and HP, manifesting that PDHP as insulating substrate inhibits the electron transfer to a great extent. A well-documented pair of quasireversible one-electron redox peaks is clearly displayed on PDHP and $Cu_2(NDC)_2$/PDHP. Compared to bulk $Cu_2(NDC)_2$, dramatically enhanced peak current (i_p) and reduced peak potential separation (E_p) are distinctively exhibited on $Cu_2(NDC)_2$/PDHP, suggestive of improved electrochemical activities. Randles–Sevcik equation,[40] $i_p = 2.69 \times 10^5\ n^{3/2}\ AD^{1/2}\ \nu^{1/2}\ c$ ($D = 6.3 \times 10^{-6}$ cm s^{-1}) is used to estimate the electrochemical active surface areas (EASAs) of $Cu_2(NDC)_2$/PDHP. The calculation values are 3.18, 1.32, and 0.30 cm^{-2} for $Cu_2(NDC)_2$/PDHP, PDHP, and bulk $Cu_2(NDC)_2$. This result reveals that synthetic Murray $Cu_2(NDC)_2$/PDHP greatly enhances the EASAs and favors the efficient electron transfer.

The effects of different scan rates at $Cu_2(NDC)_2$/PDHP are further investigated to better elucidate the fast electron transfer. Well-displayed redox peaks at −0.2/−0.58, 0.35/−0.1, and 0.75 V are corresponding to respective conversion of Cu(0)–Cu(I), Cu(I)–Cu(II), and Cu(II)–Cu(III). The redox peaks (I and II) of $Cu_2(NDC)_2$/PDHP are shifted toward more positive and negative potentials, implying a quasireversible process. Because of nonobvious cathodic peak at 0.65 V, conversion of Cu(II)–Cu(III) can be considered as a nonreversible process. The inset of Figure 3C presents that redox peak currents linearly increase as square root of scan rate, suggesting a diffusion-controlled process. Based upon Laviron's equation, the electron-transfer coefficient (α) and electron-transfer rate (k_s) are achieved.[41]

$$E_{pa} = E^0 + \frac{RT}{(1-\alpha)nF} + \frac{RT}{(1-\alpha)nF}\ln \nu \quad (1)$$

$$E_{pc} = E^0 + \frac{RT}{\alpha nF} - \frac{RT}{\alpha nF}\ln \nu \quad (2)$$

where R, F, and T are the gas constant, Faraday constant, and temperature in Kelvin, respectively (R = 8.314 J mol^{-1} K^{-1}, F = 96 500 C mol^{-1}, T = 298 K). In the light of the plots of redox peak potential (E_{pa} and E_{pc}) versus natural logarithm of scan rate (Figure 3D), α and n for Cu(0)–Cu(I) and Cu(I)–Cu(II) are, respectively, computed as 0.62 and 1, 0.58 and 1, which implies single-electron transfer. As for Cu(II)–Cu(III), the $(1-\alpha)n$ can be obtained by calculating the slopes from the linear relationship between E_{pa} and lnν. For totally irreversible diffusion-controlled process, the number of electrons (n) can be obtained according to the following equation[41]

$$\left|E_p - E_{\frac{p}{2}}\right| = \left(\frac{47.7}{\alpha n}\right) \quad (3)$$

From the above equations, α and n are 0.57 and 1, respectively. And, the electron transfer rate k_s for Cu(0)–Cu(I), Cu(I)–Cu(II), and Cu(II)–Cu(III) could be evaluated by Laviron's equation when $n\triangle E_p > 200$ mV.[41]

$$k_s = \frac{\alpha nF\nu}{RT} \quad (4)$$

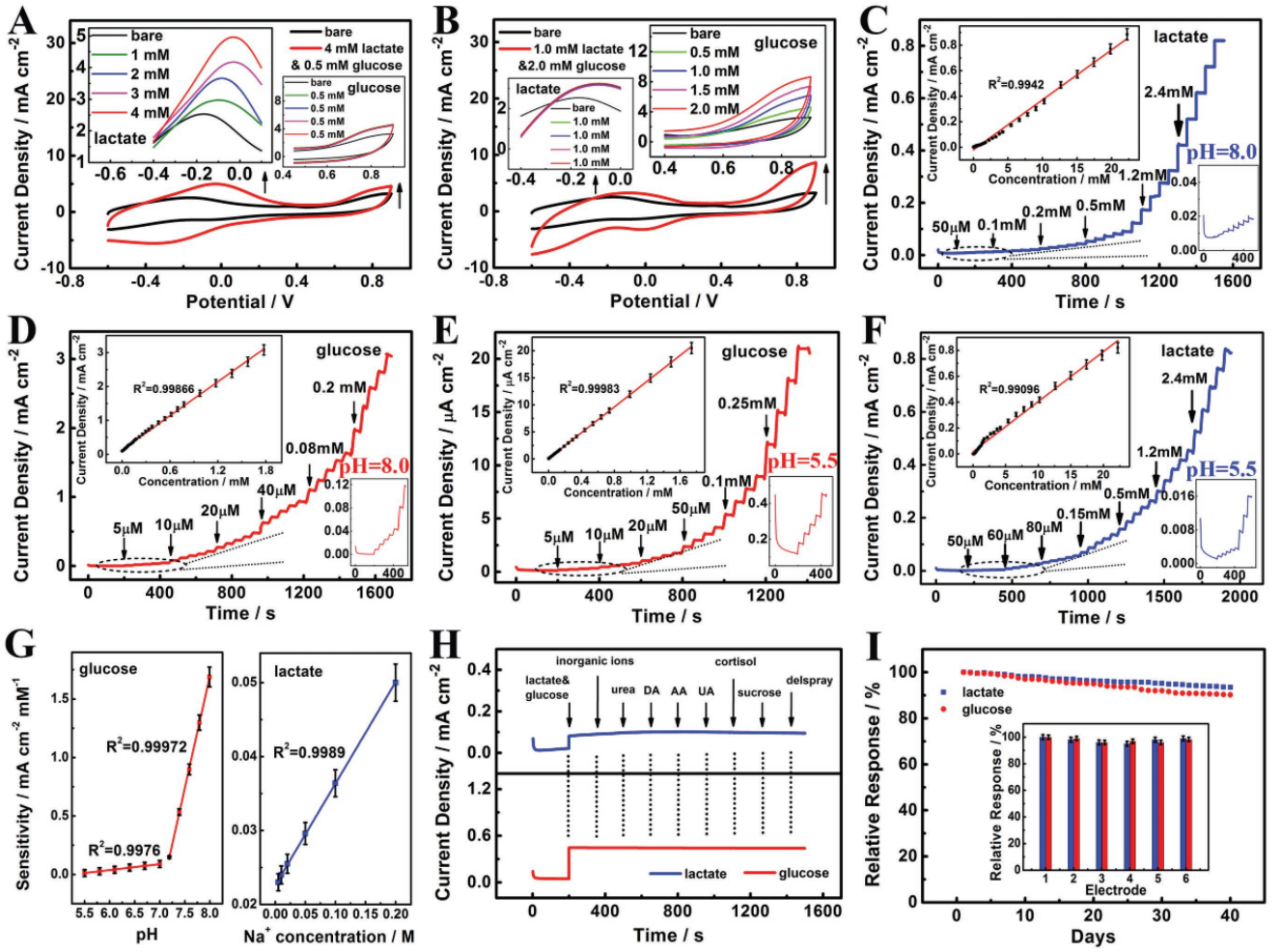

Figure 4. A,B) Cyclic voltammogram of $Cu_2(NDC)_2$/PDHP electrode in simulated sweat (pH = 8.0) with analytes. Inset: CV responses of $Cu_2(NDC)_2$/PDHP with different concentrations of analytes at 50 mV s^{-1}. Current responses of $Cu_2(NDC)_2$/PDHP to successive injection of C) lactate, D) glucose in stirring simulated sweat (pH = 8.0). Inset: the corresponding calibration curve. Current responses of $Cu_2(NDC)_2$/PDHP to successive injection of E) glucose, F) lactate in stirring simulated sweat (pH = 5.5). Inset: the corresponding calibration curve. G) Calibration curve of sensitivity versus pH for glucose and C_{Na^+} for lactate. H) Influence of interferences on the simultaneous response lactate and glucose. I) Stability of $Cu_2(NDC)_2$/PDHP electrode. Inset: current response of six different $Cu_2(NDC)_2$/PDHP.

The results were, respectively, calculated to be 1.21, 1.13, and 1.11 s^{-1} at 50 mV s^{-1}. These data fully demonstrate very efficient electron transfer in biomimetic Murray MOF film (see comparison with other films in the Supporting Information).

2.3. Bifunctional Sensing Performances of $Cu_2(NDC)_2$/PDHP

Figure 4A,B presents the CV responses of $Cu_2(NDC)_2$/PDHP toward lactate and glucose with different concentrations in simulated sweat. Obviously, when the glucose concentration is fixed, the oxidation peak current density of lactate displays a dramatical increase with the lactate concentration increasing and vice versa. This charming result reveals that the responses to lactate and glucose are independent of each other. Next, the sensing performances including sensitivity, linear range, and detection limit also have been investigated to better understand the high activity of mass transfer of $Cu_2(NDC)_2$/PDHP. Figure 4C,D summarizes the current responses toward lactate and glucose at the optimal potential of –0.2 and 0.75 V, respectively (see Figures S3–S10 in the Supporting Information). The current densities gradually increase with successive step increments of analyte concentrations and steady-state current signals are collected within 5 s. The corresponding linear relationship between current densities and analyte concentrations indicates a wide linear dynamic range over the concentration from 0.05×10^{-3} to 22.25×10^{-3} M for lactate and 5×10^{-6} to 1.775×10^{-3} M for glucose (insets of Figure 4C,D), with high sensitivities and low detection limit (a signal-to-noise ratio of 3:1) of 0.0359 mA cm^{-2} mM^{-1}, 25×10^{-6} M for lactate and 1.69 mA cm^{-2} mM^{-1}, 2×10^{-6} M for glucose, respectively. Using the Murray network inspired from natural system, the superb bifunctional sensing performances of $Cu_2(NDC)_2$/PDHP outperform that of bulk $Cu_2(NDC)_2$ (see Figure S2 in the Supporting Information). Also, the proposed $Cu_2(NDC)_2$/PDHP is comparable or superior to many reported electrochemical

sensors based on different nanohybrid materials (see Table S1 in the Supporting Information).

Cu-based materials generally do not determinate the glucose in acid or neutral media because the production of sensing element (Cu(III)) is greatly dependent on the OH^- concentration in electrolyte.[42] An unexpected, interesting discovery in our work is that $Cu_2(NDC)_2$/PDHP possesses moderate glucose sensing ability in acid media. The current–time plot for the glucose in weak acid simulated sweat (pH = 5.5) is depicted in Figure 4E. Well-defined steady-state amperometric current responses are achieved within 5 s, and the current densities increase stepwise with successive additions of glucose. The current density displays a linear relationship with the glucose concentrations from 5×10^{-6} to 1.74×10^{-3} M, and the sensitivity and detection limit are 12.1 μA cm^{-2} mM^{-1} and 3×10^{-6} M, respectively (inset of Figure 4E). But for lactate, acid environment does not decrease the lactate sensing performances of $Cu_2(NDC)_2$/PDHP including sensitivity, linear range, and detection limit, revealing different sensing mechanisms between glucose and lactate. Na^+ transfer should dominate the lactate sensing performance of $Cu_2(NDC)_2$/PDHP. Figure 4G summarizes the relationship between sensitivity and influencing factor. The sensing mechanism of lactate and glucose can be summarized.

For lactate

$$\left\{Cu^{II}NDC\right\}_m + mNa^+ + me^- \rightarrow \left\{Cu^{I}\left(Na^+\right)NDC\right\}_m \tag{5}$$

$$\left\{Cu^{I}\left(Na^+\right)NDC\right\}_m + \text{lactate} + 2Na^+ \rightarrow \left\{Cu^{I}_{1-\frac{2}{m}}\left(Cu^0\right)_{\frac{2}{m}}\left(Na^+\right)_{1+\frac{2}{m}}NDC\right\}_m + \text{pyruvate} \tag{6}$$

$$\left\{Cu^{I}_{1-\frac{2}{m}}\left(Cu^0\right)_{\frac{2}{m}}\left(Na^+\right)_{1+\frac{2}{m}}NDC\right\}_m \rightarrow \left\{Cu^{I}\left(Na^+\right)NDC\right\}_m + 2Na^+ + 2e^- \tag{7}$$

For glucose

$$\left\{Cu^{II}NDC\right\}_m + mH_2O \rightarrow \left\{Cu^{III}NDC\cdot OH\right\}_m + me^- \tag{8}$$

$$\frac{2}{m}\left\{Cu^{III}NDC\cdot OH\right\}_m + \text{glucose} \rightarrow \frac{2}{m}\left\{Cu^{II}NDC\right\}_m + \text{gluconolactone} \tag{9}$$

For lactate sensing, in $Cu_2(NDC)_2$/PDHP, between adjacent redox centers, electron hopping occurs accompanied with diffusion of charge-balancing electrolyte counterions. The Na^+ ions are relatively free to move across the hierarchical channels since the diffusions of Na^+ is faster than charge mobility. Thus, those unconstrained Na^+ and electrons make the oxidized centers along the 3D interface quickly expose and catalyze lactate. The coordination environment not only improves electronic coupling between neighboring metal centers but also maximizes the metal–ligand π-orbital overlap and minimizes reorganization energy of electron transfer. As for glucose detection, the mechanism could be described as following: the heteroepitaxy growth ensures precise self-assembly of $Cu_2(NDC)_2$ and the oxygen atoms in linker with lone pair electrons can serve as Lewis basic sites. These sites have a tendency to combine with protons, and hence create a relative microenvironment. On the other hand, during the self-assembly process, few Cu(II) are also coordinated with the oxygen donor atoms in H_2O. But, the small water molecules will be removed during the drying process, which leaves many open, unsaturated metal sites. Moreover, high surface energy of these active sites would drive them to quickly absorb OH^-. Consequently, some OH^- are produced in the Cu(III) center at high potential, which will catalyze glucose.

To investigate the anti-interference of $Cu_2(NDC)_2$/PDHP for lactate and glucose detection, the interference including Na^+, K^+, Ca^{2+}, Mg^{2+}, Al^{3+}, Ba^{2+}, Zn^{2+}, Co^{2+}, Ni^{2+}, Mn^{2+}, NH_4^+, Cl^-, SO_4^{2-}, CO_3^{2-}, HCO_3^-, PO_4^-, HPO_4^{2-}, $H_2PO_4^-$, NO_3^-, urea, dopamine (DA), ascorbic acid (AA), uric acid (UA), cortisol, sucrose, and delspray on simultaneous response of analytes has been monitored by amperometric measurement (Figure 4H). Due to the inherent specificity of $Cu_2(NDC)_2$, no significant change occurs in the current response of lactate and glucose after adding equal amount of interfere even the potential for glucose detection is relative high. This result illustrates the excellent selectivity of $Cu_2(NDC)_2$/PDHP. Furthermore, long-time stability and reproducibility of $Cu_2(NDC)_2$/PDHP also have been evaluated through monitoring current responses of 1×10^{-3} M lactate and glucose on the same electrode and six replicates of 1×10^{-3} M lactate and glucose on one electrode, respectively (Figure 4I). The relative standard deviation (RSD) values are less than 5%, suggestive of the favorable long-time stability and reproducibility of $Cu_2(NDC)_2$/PDHP. In addition to being highly efficient, our $Cu_2(NDC)_2$/PDHP is also of low cost for repeated reactions.

2.4. Network Matrix in $Cu_2(NDC)_2$/PDHP

Based upon above evaluation of electrocatalytic activity, another interesting question arises: why do the Murray MOFs possess high electrochemical sensing performances? Reasonable structure design serves an explanation for minimizing of transport resistance of the whole pores and fast transfer of analytes, ions, and electrons. We have built the network matrix model with multiple channels from Murray MOFs (**Figure 5**A) and investigated the effect of channel numbers on transport efficiency in this architecture. To deeply comprehend biomimetic Murray MOF network matrix, a mathematical optimization is proposed, aiming at understanding the flow transfer resistance in $Cu_2(NDC)_2$/PDHP (Figure 5A). According to the transport channel self-similarity[43]

$$R(\text{Ma},m,M) = M^{-2}\left[f(\text{Ma},m,M)\right]\left[g(\text{Ma},m,M)\right] \tag{10}$$

$$f(\text{Ma},m,M) = \left[1+2\sum_{j=2}^{\text{Ma}}\left(\frac{\text{Ma}-j+1}{\text{Ma}}\right)^{\frac{1}{2}}\right]\frac{1}{2m} + \left[1+2\sum_{j=2}^{\text{Ma}}\left(\frac{m-j+1}{m}\right)^{\frac{1}{2}}\right]T(m,M) \tag{11}$$

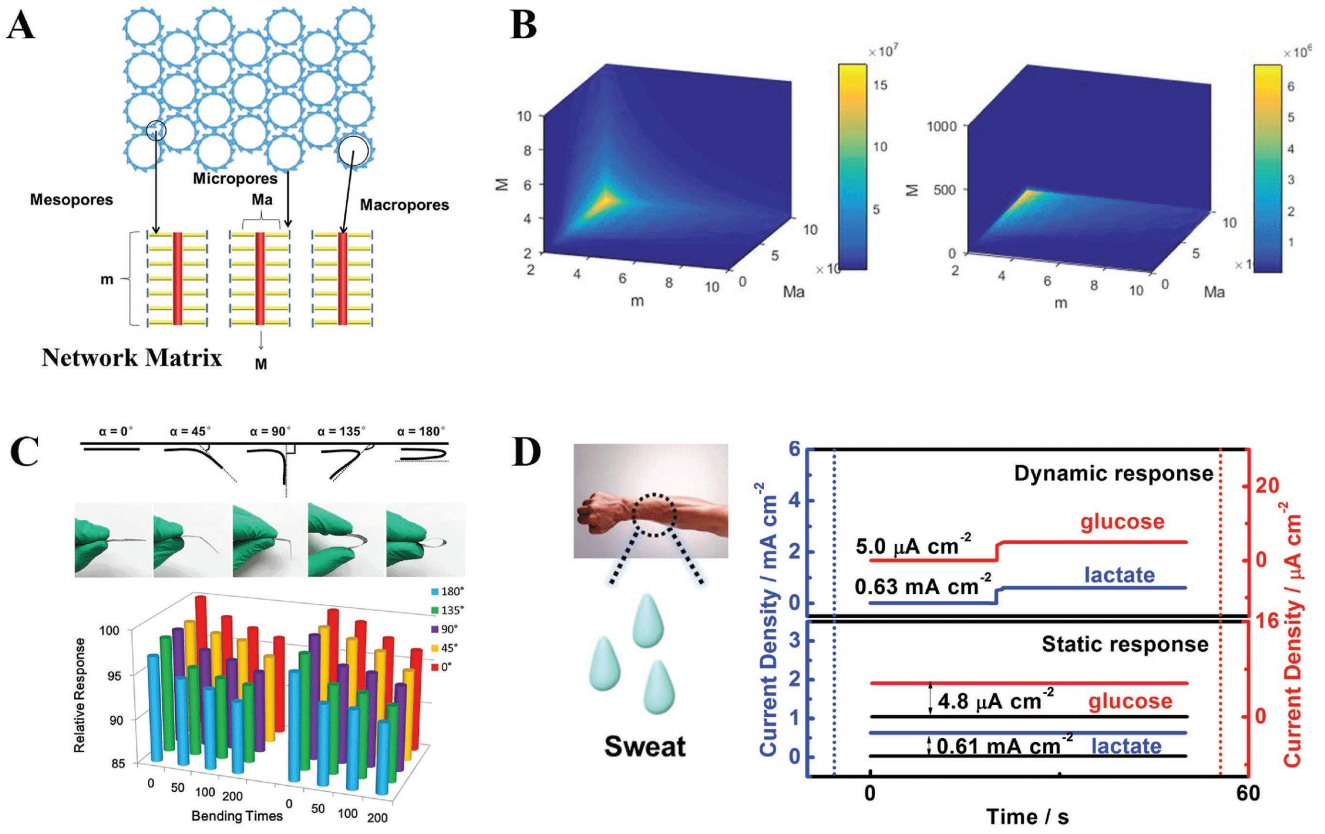

Figure 5. A) Network matrix. B) 4D-visualized function diagram $R(\mathrm{Ma}, m, M)$. C) Flexibility test after bending different times and angles. D) Dynamic and static sweat sensing evaluation.

$$g(\mathrm{Ma},m,M)=\left[1+2\sum_{j=2}^{\mathrm{Ma}}\left(\frac{\mathrm{Ma}-j+1}{\mathrm{Ma}}\right)^{\frac{3}{2}}\right]\frac{1}{2m}+\left[1+2\sum_{j=2}^{\mathrm{Ma}}\left(\frac{m-j+1}{m}\right)^{\frac{3}{2}}\right]T(m,M) \tag{12}$$

$$T(m,M)=\frac{(2m)^{-2}-(2m)^{-1}\left(10^{-4}\right)M}{1-(2m)^{-1}}+\frac{(2m)^{-1}-(2m)^{-1}\left(10^{-4}\right)M}{2\left[1-(2m)^{-1}\right]} \tag{13}$$

where R is the total potential drop through channel work, demonstrating the total flow resistance of transport channel work; M is the number of first-order transport channel (macropores); Ma is the number of subchannels (mesopores) of first-order transport channel; m is the number of one transport subchannel (micropores) (see details in the Supporting Information). Considering that R is the function of three variables, a 4D-visualized function diagram depicts the relevance between total flow resistance of transport channel work and Ma, m, and M (Figure 5B). The change in color manifests the value of total transfer resistance. The color from yellow to blue means the resistance from high to low level. In the left figure in Figure 5B, when M is very small, it is can be observed that R is very high (yellow part). But with M increasing, the color gradually becomes bluer, implying that the resistance dramatically decreases, as shown in the right figure in Figure 5B. It proves that the number of macropores dominates decreasing resistance rather than the number of mesopores and micropores. Also, in $Cu_2(NDC)_2$/PDHP, centimeter-scaled distribution of macropores ensures millions of macropores and thousands of mesopores and micropores, effectively reducing the transfer resistance. On the other hand, we define ΔC and ΔV as the concentration and potential difference across the pore, respectively; D and σ are, respectively, the diffusion coefficient and conductivity; Q_1 and Q_2 are the amount of analytes diffused and electron transferred through a cross-section per unit time, respectively. For mass diffusion, ionic or electronic transfer in $Cu_2(NDC)_2$/PDHP[15,44]

$$Q_1 = D\pi r^2 \frac{\Delta C}{l} \tag{14}$$

$$Q_2 = \sigma\pi r^2 \frac{\Delta V}{l} \tag{15}$$

A Lagrange multiplier λ is introduced to minimize the entransy dissipation rate. In the light of Murray's principle

$$\frac{\partial(Q_1\Delta C-\lambda V)}{\partial r}=0 \tag{16}$$

$$\frac{\partial(Q_2\Delta V-\lambda V)}{\partial r}=0 \tag{17}$$

Consequently, $Q_1 = b_1 r^2$, $Q_2 = b_2 r^2$, where b_1 and b_2 are constants (see details in the Supporting Information). Further, we define Q_m as amounts of substances imported into the macrospores or the electrons and ions transferred through the cross-section per unit time. The law gives for connecting macrospores with radius of r to subpores with radius of r_i for mass, electron, or ion transfer.

$$Q_m = \sum_{i=1}^{N} Q_i \tag{18}$$

$$r^2 = \sum_{i=1}^{N} r_i^2 \tag{19}$$

From derivation of formula, Q_m is proportional to the electrochemical reaction rate. Also, it reveals that fast diffusion rates of analyte, ion, and electron transfer depend on the appropriate size and reasonable distribution of pores.

2.5. Sweat Sensing Evaluation

Motivated on outstanding sensing performances and transfer mechanism of biomimetic Murray MOFs, it is highly desirable to apply $Cu_2(NDC)_2$/PDHP in the sweat lactate and glucose sensing platform. And for wearable sweat sensors, flexibility substrate plays crucial roles in real-time monitoring during continuous movement.[38,45,46] The mechanical stability of $Cu_2(NDC)_2$/PDHP at different bending states has been studied. The amperometric responses to 1×10^{-3} M lactate and glucose on $Cu_2(NDC)_2$/PDHP at the widest bending angle after 200 bending times are 93.1% and 92.5% of that at normal state (Figure 5C). This demonstrates that bending-induced mechanical stress has no impact on the sensing performances due to excellent flexibility, high toughness and stiffness of PDHP, and superb adhesion of $Cu_2(NDC)_2$ deposited on it.

Next, $Cu_2(NDC)_2$/PDHP is characterized in simulated sweat without lactate and glucose operated at a potential of −0.20 and +0.75 V for dynamic measurement (Figure 5D). Dynamic measurement demonstrates a dynamic, fast, and instantaneous response. The pH and Na^+ concentrations of fresh sweat are 5.5 and 0.09 M, respectively. When 100 µL sweat is added into electrolyte, distinct current responses toward sweat lactate and glucose are observed. From the linear relationship between current density and concentration of analytes, sensitivity, and impact factors, the concentration of sweat lactate and sweat glucose are calculated to be 14.9×10^{-3} and 0.4×10^{-3} M, respectively. Further, given wearable sweat sensing is working in a static manner without using the electrolyte, the static test is carried out to directly measure perspiration for more accurate sweat response. Static measurement is carried out in the case where analyte is already in electrolyte rather than quick addition in electrolyte. It gives static and accumulative but not instantaneous responses. The concentrations from static responses are 14.5×10^{-3} and 0.385×10^{-3} M, respectively. Compared with dynamic response, static response is relatively smaller due to concentration polarization. The electrochemical analysis method utilizing $Cu_2(NDC)_2$/PDHP also has been calibrated with the traditional, standard ultraviolet spectrophotometry, further confirming that our proposed approach is credible (see Figures S11–S13 and Table S2 in the Supporting Information).

3. Conclusions

In summary, we have proposed a coffee ring–inspired approach toward oriented self-assembly of biomimetic Murray MOFs, $Cu_2(NDC)_2$/PDHP. This versatile method integrates two types of self-assembly, evaporation-driven and heteroepitaxy self-assembly, offering a facile, modular, and economic strategy to fabricate large-area, oriented packed MOF film. The rational, predictable design based on Murray's law endows MOF film with hierarchical pores and significantly improves its electrochemical activity. The proposed network matrix fully elucidates the relationship between transfer principle and micro-, meso-, and macropores in $Cu_2(NDC)_2$/PDHP. The excellent sweat sensing performances including high sensitivity and selectivity, wide testing range, as well as long-time stability offer it possibility to be applied in next generation of wearable sweat biosensors. We profoundly believe that our coffee ring–inspired approach would provide a new insight into on designing porous MOF film and other MOF-based functional nanomaterials. It is also envisioned that the integration of big-data techniques, wireless technology, along with our biomimetic Murray strategy paves the way of next generation of MOF-based wearable electronics for a healthy and sustainable future.

4. Experimental Section

Synthesis of $Cu_2(NDC)_2$/PDHP: Before pencil painting, normal A4 paper (2 cm × 2 cm) was treated by hydrophobicity modification. 50 mg mL^{-1} of isotactic PP was first dissolved in the stirring dimethylbenzene (30 mL) for 20 min under 90 °C. Then, 6 mL acetone was added in the transparent solution and kept stirring for 2 min. The piece of A4 paper was immersed in the solution for 30 s and pulled out to dry. Due to the phase separation, PP accumulated and deposited on the surface of A4 paper. The paper was denoted as HP. After that, the 9B pencil was used to draw, leaving the graphite as few layers on the surface of HP. The PDHP was obtained as the conductive substrate.

0.15 M $NH_3 \cdot H_2O$ (3 mL) was prepared and added dropwise into solution containing 0.05 M $CuSO_4$ (10 mL). And, 10 M NaOH (0.3 mL) was slowly dropped to maintain reaction mixture and kept stirring 40 min at room temperature. The addition of excess hydroxide ions can gradually convert the $[Cu(NH_3)_4]^{2+}$ transient complex species into less soluble $Cu(OH)_2$. The as-prepared nanowires were centrifuged and washed for several times to obtain light-blue nanocrystalline product. Dichloromethane was selected as the solvent for coffee ring forming. Dichloromethane (3 mL) containing $Cu(OH)_2$ nanowires dripped on PDHP surface. After fast evaporation of dichloromethane, the blue powders were deposited on the surface, forming coffee ring. $Cu(OH)_2$/PDHP was obtained through repetition of this step. After that, $Cu(OH)_2$/PDHP was immersed in the ethanol solution of 0.05 g $H_2(NDC)$ for 40 min. Finally, the as-prepared paper was washed with excess ethanol to remove residual $H_2(NDC)$, denoted as $Cu_2(NDC)_2$/PDHP.

Electrochemical Measurement: A three-electrode system was performed with Pt, Ag/AgCl, nanohybrid as counter electrode, reference electrode, and working electrode, respectively. For electrochemical behavior test, EIS test frequency was 0.1–10^5 Hz and CV scan rate was 50 mV s^{-1}. For sensing performance test, potential was set at −0.2 and +0.75 V for lactate and glucose detection, respectively. The electrolyte-simulated sweat contained 0.1 M NaCl and 1×10^{-6} M urea. 2 mm space

was set in PDHP and workstation within twin channel supported the bifunctional and simultaneous detection. The human perspiration was collected from a healthy volunteer who had 2 h of continuous exercise. The first author Zhengyun Wang as a volunteer was recruited for collecting sweat in the study, and informed consent was obtained from the individual. See more details in the Supporting Information.

Supporting Information

Supporting Information is available from the Wiley Online Library or from the author.

Acknowledgements

This research was supported by the National Key Research and Development Program of China, (Grant No. 2018YFF0215002), the National Natural Science Foundation of China (Grant No. U1662114), the Independent Innovation Research Fund of Huazhong University of Science and Technology (Grant No. 2017KFYXJJ164), the Foundation of Hubei Key Laboratory of Material Chemistry and Service Failure (Grant Nos. 201502, 201702), and the Key Laboratory of Material Chemistry for Energy Conversion and Storage, Ministry of Education (2018).

Conflict of Interest

The authors declare no conflict of interest.

Keywords

coffee ring, Murray MOF network, oriented self-assembly, sweat biosensor

Received: July 9, 2018
Revised: September 6, 2018
Published online:

[1] C. Doonan, R. Riccò, K. Liang, D. Bradshaw, P. Falcaro, *Acc. Chem. Res.* **2017**, *50*, 1423.
[2] I. Stassen, N. Burtch, A. Talin, P. Falcaro, M. Allendorf, R. Ameloot, *Chem. Soc. Rev.* **2017**, *46*, 3185.
[3] A. Knebel, C. Zhou, A. Huang, J. Zhang, L. Kustov, J. Caro, *Chem. Eng. Technol.* **2018**, *41*, 224.
[4] M. X. Wu, Y. W. Yang, *Adv. Mater.* **2017**, *29*, 1606134.
[5] J. Duan, S. Chen, C. Zhao, *Nat. Commun.* **2017**, *8*, 15341.
[6] Y.-B. Huang, J. Liang, X.-S. Wang, R. Cao, *Chem. Soc. Rev.* **2017**, *46*, 126.
[7] H. He, J. A. Perman, G. Zhu, S. Ma, *Small* **2016**, *12*, 6309.
[8] V. Stavila, C. Schneider, C. Mowry, T. R. Zeitler, J. A. Greathouse, A. L. Robinson, J. M. Denning, J. Volponi, K. Leong, W. Quan, M. Tu, R. A. Fischer, M. D. Allendorf, *Adv. Funct. Mater.* **2016**, *26*, 1699.
[9] S. Sachdeva, M. R. Venkatesh, B. E. Mansouri, J. Wei, A. Bossche, F. Kapteijn, G. Q. Zhang, J. Gascon, L. C. P. M. de Smet, E. J. R. Sudhölter, *Small* **2017**, *13*, 1604150.
[10] S. Alizadeh, D. Nematollahi, *J. Am. Chem. Soc.* **2017**, *139*, 4753.
[11] J. Liu, C. Woll, *Chem. Soc. Rev.* **2017**, *46*, 5730.
[12] P. Falcaro, K. Okada, T. Hara, K. Ikigaki, Y. Tokudome, A. W. Thornton, A. J. Hill, T. Williams, C. Doonan, M. Takahashi, *Nat. Mater.* **2017**, *16*, 342.
[13] C. D. Murray, *Proc. Natl. Acad. Sci. USA* **1926**, *12*, 207.
[14] T. F. Sherman, *J. Gen. Physiol.* **1981**, *78*, 431.
[15] X. D. Shan, M. Wang, Z. Y. Guo, *Math. Probl. Eng.* **2011**, *2011*, 1.
[16] A. Bejan, S. Lorente, *J. Appl. Phys.* **2013**, *113*, 151301.
[17] K. A. McCulloh, J. S. Sperry, F. R. Adler, *Nature* **2003**, *421*, 939.
[18] X. Zheng, G. Shen, C. Wang, Y. Li, D. Dunphy, T. Hasan, C. J. Brinker, B.-L. Su, *Nat. Commun.* **2017**, *8*, 14921.
[19] T. Rodenas, I. Luz, G. Prieto, B. Seoane, H. Miro, A. Corma, F. Kapteijn, F. X. Llabrés i Xamena, J. Gascon, *Nat. Mater.* **2015**, *14*, 48.
[20] Y. Yoo, H.-K. Jeong, *Chem. Commun.* **2008**, 2441.
[21] E. Biemmi, C. Scherb, T. Bein, *J. Am. Chem. Soc.* **2007**, *129*, 8054.
[22] W.-J. Li, M. Tu, R. Cao, R. A. Fischer, *J. Mater. Chem. A* **2016**, *4*, 12356.
[23] A. Schoedel, C. Scherb, T. Bein, *Angew. Chem., Int. Ed.* **2010**, *49*, 7225.
[24] O. Shekhah, L. Fu, R. Sougrat, Y. Belmabkhout, A. J. Cairns, E. P. Giannelis, M. Eddaoudi, *Chem. Commun.* **2012**, *48*, 11434.
[25] H. Wei, L. Zhiqun, *Angew. Chem., Int. Ed.* **2012**, *51*, 1534.
[26] H. Hu, R. G. Larson, *J. Phys. Chem. B* **2006**, *110*, 7090.
[27] S. Anastasova, B. Crewther, P. Bembnowicz, V. Curto, H. M. D. Ip, B. Rosa, G.-Z. Yang, *Biosens. Bioelectron.* **2017**, *93*, 139.
[28] W. Gao, S. Emaminejad, H. Y. Y. Nyein, S. Challa, K. Chen, A. Peck, H. M. Fahad, H. Ota, H. Shiraki, D. Kiriya, D.-H. Lien, G. A. Brooks, R. W. Davis, A. Javey, *Nature* **2016**, *529*, 509.
[29] S. Nakata, T. Arie, S. Akita, K. Takei, *ACS Sens.* **2017**, *2*, 443.
[30] S. Wang, Y. Wu, Y. Gu, T. Li, H. Luo, L.-H. Li, Y. Bai, L. Li, L. Liu, Y. Cao, H. Ding, T. Zhang, *Anal. Chem.* **2017**, *89*, 10224.
[31] Z. Deng, H. Jiang, Y. Hu, Y. Liu, L. Zhang, H. Liu, C. Li, *Adv. Mater.* **2017**, *29*, 1603020.
[32] V. A. T. Dam, M. A. G. Zevenbergen, R. van Schaijk, *Sens. Actuators, B* **2016**, *236*, 834.
[33] P. J. Derbyshire, H. Barr, F. Davis, S. P. J. Higson, *J. Physiol. Sci.* **2012**, *62*, 429.
[34] M. Onor, S. Gufoni, T. Lomonaco, S. Ghimenti, P. Salvo, F. Sorrentino, E. Bramanti, *Anal. Chim. Acta* **2017**, *989*, 80.
[35] Z. Wang, S. Dong, M. Gui, M. Asif, W. Wang, F. Wang, H. Liu, *Anal. Biochem.* **2018**, *543*, 82.
[36] M. S. Talary, F. Dewarrat, D. Huber, A. Caduff, *J. Non-Cryst. Solids* **2007**, *353*, 4515.
[37] S.-D. Seo, Y.-H. Jin, S.-H. Lee, H.-W. Shim, D.-W. Kim, *Nanoscale Res. Lett.* **2011**, *6*, 397.
[38] L. Wang, Y. Dong, Y. Zhang, Z. Zhang, K. Chi, H. Yuan, A. Zhao, J. Ren, F. Xiao, S. Wang, *NPG Asia Mater.* **2016**, *8*, e337.
[39] X. Huang, P. Sheng, Z. Tu, F. Zhang, J. Wang, H. Geng, Y. Zou, C.-a. Di, Y. Yi, Y. Sun, W. Xu, D. Zhu, *Nat. Commun.* **2015**, *6*, 7408.
[40] A. J. Bard, L. R. Faulkner, in *Electrochemical Methods: Fundamentals and Applications*, 2nd ed. Wiley, New York **2001**, p. 96.
[41] E. Laviron, *J. Electroanal. Chem. Interfacial Electrochem.* **1979**, *101*, 19.
[42] Y. Liu, Y. Zhang, J. Chen, H. Pang, *Nanoscale* **2014**, *6*, 10989.
[43] L. Hu, D. Wang, H. Zhu, T. Fan, *Int. J. Heat Mass Transfer* **2018**, *119*, 20.
[44] X. B. Liu, M. Wang, J. Meng, E. Ben-Naim, Z. Y. Guo, *Int. J. Nonlinear Sci. Numer. Simul.* **2010**, *11*, 113.
[45] F. Xiao, L. Wang, H. Duan, *Biotechnol. Adv.* **2016**, *34*, 234.
[46] Z. Wang, M. Gui, M. Asif, Y. Yu, S. Dong, H. Wang, W. Wang, F. Wang, F. Xiao, H. Liu, *Nanoscale* **2018**, *10*, 6629.